ACSNANO

www.acsnano.org

ARTICLE

Polarization Control of Morphological Pattern Orientation During Light-Mediated Synthesis of Nanostructured Se–Te Films

Azhar I. Carim,[†] Nicolas A. Batara,[‡] Anjali Premkumar,[‡] Harry A. Atwater,[‡,§,∥] and Nathan S. Lewis*[,†,§,∥,⊥]

[†]Division of Chemistry and Chemical Engineering, [‡]Division of Engineering and Applied Sciences , [§]The Joint Center for Artificial Photosynthesis, [∥]Kavli Nanoscience Institute, and [⊥]Beckman Institute California Institute of Technology, Pasadena, California 91125, United States

ABSTRACT: The template-free growth of well ordered, highly anisotropic lamellar structures has been demonstrated during the photoelectrodeposition of Se–Te films, wherein the orientation of the pattern can be directed by orienting the linear polarization of the incident light. This control mechanism was investigated further herein by examining the morphologies of films grown photoelectrochemically using light from two simultaneous sources that had mutually different linear polarizations. Photoelectrochemical growth with light from two nonorthogonally polarized same-wavelength sources generated lamellar morphologies in which the long axes of the lamellae were oriented parallel to the intensity-weighted average polarization orientation. Simulations of light scattering at the solution–film interface were consistent with this observation. Computer modeling of these growths using combined full-wave electromagnetic and Monte Carlo growth simulations successfully reproduced the experimental morphologies and quantitatively agreed with the pattern orientations observed experimentally by considering only the fundamental light-material interactions during growth. Deposition with light from two orthogonally polarized same-wavelength as well as different-wavelength sources produced structures that consisted of two intersecting sets of orthogonally oriented lamellae in which the relative heights of the two sets could be varied by adjusting the relative source intensities. Simulations of light absorption were performed in analogous, idealized intersecting lamellar structures and revealed that the lamellae preferentially absorbed light polarized with the electric field vector along their long axes. These data sets cumulatively indicate that anisotropic light scattering and light absorption generated by the light polarization produces the anisotropic morphology and that the resultant morphology is a function of all illumination inputs despite differing polarizations.

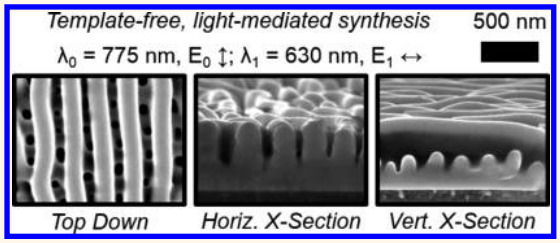

KEYWORDS: *electrodeposition, photoelectrochemistry, photodeposition, template-free, maskless, chalcogenide*

Photolithography, a technique used extensively to generate patterned materials and specifically in the semiconductor industry and in the production of integrated circuits, utilizes a photomask to spatially localize photochemical reactions to construct defined patterns.[1−3] Manipulation of the polarization of the light is another control mechanism that can be utilized to direct photodriven processes and produce targeted structures. Linearly polarized light can effect photopolymerization and/or photoalignment in liquid crystal systems, generating highly anisotropic structures oriented along or perpendicular to the electric field vector.[4−7] The photoinduced mass transport of photoisomerizable polymers in the immediate vicinity of Au or Ag nanoparticles can generate patterns in the subwavelength regime with an anisotropy dictated by the polarization of the light source.[8−11] Additionally, plasmon-mediated growth of surface-affixed triangular Ag nanoparticles during illumination with linearly polarized light results in spontaneous anisotropic orientation as well as consistent particle size.[12] This synthetic process is governed by the anisotropies in the light-material interactions resulting from sensitivity to both the wavelength and polarization of the illumination, and thus provides for the maskless generation of uniform, oriented nanostructures.[13]

Recently, the photoelectrochemical growth of semiconducting Se–Te films using linearly polarized illumination has been shown to produce highly anisotropic, nanoscale lamellar patterns in which the orientation of the patterns is correlated with the electric field vector of the incident light.[14] Such structures were formed without the use of any physical or chemical templating agents nor the use of a photomask.[15−20] Rather, in analogy to the case of the plasmon-mediated growth of Ag nanostructures, patterning resulted spontaneously due to inherent anisotropies in the light-material interactions during film growth. In this work, the patterns generated in photo-

Received: August 17, 2015
Accepted: November 22, 2015
Published: November 23, 2015

DOI: 10.1021/acsnano.5b05119
ACS Nano 2016, 10, 102–111

electrochemically grown Se−Te films utilizing two light sources with unique linear polarizations were investigated to understand the material growth response to the tailored excitation, as well as to identify strategies for obtaining morphology control and for generating three-dimensional morphological complexity. Films were generated using two same-wavelength sources with an array of polarization vector pairs as well as intensity ratios, and with two orthogonally polarized different-wavelength sources that had a series of intensity ratios. The resulting film morphologies were assessed by scanning electron microscopy. Computational modeling of the light-material interactions during photoelectrochemical growth successfully reproduced the experimentally observed morphologies. Additional modeling of light scattering at the active film−solution interface, as well as simulations of light absorption in idealized lamellar arrays, were also performed to understand the emergence of the morphologies generated using two discrete linear polarizations of light to drive film growth.

RESULTS

Figure 1 presents representative scanning electron micrographs (SEMs) of Se−Te photoelectrodeposits that were generated by

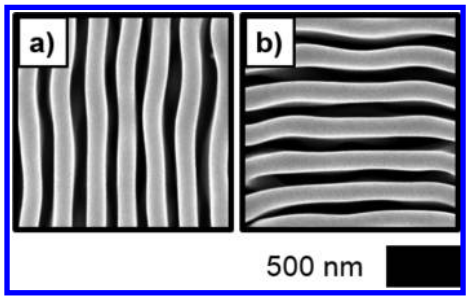

Figure 1. Effect of illumination source polarization on pattern orientation. SEMs representative of photoelectrodeposits generated with λ_{avg} = 630 nm illumination polarized (a) vertically and (b) horizontally.

electrochemically reducing SeO_2 and TeO_2 potentiostatically while illuminating the electrode with a narrowband light-emitting diode (LED) having an intensity-weighted average wavelength (λ_{avg}) of 630 nm polarized vertically (a) and horizontally (b). In both cases, a highly anisotropic, lamellar-type morphology was observed. The long axes of the lamellar structures were oriented parallel to the polarization of the illumination; hence, vertical polarization resulted in vertically oriented lamellae whereas horizontal polarization yielded horizontally oriented lamellae. X-ray diffraction analysis has shown that Se−Te photoelectrodeposits generated in this manner are nanocrystalline with crystallites composed of a substitutional alloy of Se and Te in a hexagonal structure common to both elements in their pure phases.[14]

Figure 2a−c presents SEMs representative of photoelectrodeposits generated using two equal intensity LED sources with λ_{avg} = 630 nm. One source was polarized vertically and the polarization of the second source was offset clockwise from the vertical by θ_1 = 20° (a), 40° (b), or 60° (c). In each case, a lamellar pattern was observed that was similar to the pattern produced when only a single source was utilized. The long axis of the lamellar structures rotated clockwise away from the vertical in each case, and the magnitude of this rotation (θ_{obs}) increased with increasing values of θ_1. For θ_1 = 20°, 40°, and 60°, values of θ_{obs} of 8 ± 1°, 17 ± 2°, and 28 ± 5°, respectively, were measured. Figure 2d presents a plot of the observed magnitude of the pattern rotation from the vertical (θ_{obs}) as a function of θ_1. The trend was well-fit by a line of the form $\theta_{obs} = 0.5\theta_1 - 1$. Figure 2e−g presents SEMs representative of photoelectrodeposits that were generated in a manner similar to those presented in Figure 2a. Here, θ_1 was fixed to a value of 50°, and the ratio of the intensity of this second source to the total intensity, $[I_1/(I_0 + I_1)]$, was adjusted to 0.20 (e), 0.50 (f), and 0.80 (g), respectively. Again, the long axes of the lamellar structures were rotated clockwise away from the vertical in each case, and the magnitude of this rotation (θ_{obs}) increased with increasing values of the quantity $I_1/(I_0 + I_1)$. For $I_1/(I_0 + I_1)$ = 0.20, 0.50, and 0.80, values of θ_{obs} of 10 ± 1°, 23 ± 5°, and 38 ± 3°, respectively, were observed. Figure 2h presents a plot of θ_{obs} as a function of the quantity $I_1/(I_0 + I_1)$. The trend was well-fit by a line of the form $\theta_{obs} = 0.5I_1/(I_0 + I_1) - 1$.

Figure 3 presents SEMs representative of photoelectrodeposits that were generated using two LED sources with λ_{avg} = 630 nm, with one source polarized vertically with intensity I_0 and the other polarized horizontally with intensity I_1, wherein $I_0 \neq I_1$. The intensity ratio between the horizontally polarized source and the vertically polarized source (I_1/I_0) was 1.50 (a), 2.00 (b), and 4.00 (c). In (a), a square mesh morphology was observed in which a lamellar pattern was produced with the long axes of the lamellae running horizontally, superimposed over another similar pattern in which the long axes of the lamellae ran vertically. The contrast in the SEM suggests that the vertically aligned lamellae were shorter (darker) than those running horizontally. The pattern in (b) is similar to that in (a), but the horizontally oriented lamellae appeared to increase in height relative to the lamellae that ran vertically. In (c), only horizontally running lamellae are visible, and the contrast in the SEM does not suggest the formation of any other structure.

Figure 4a−d presents a series of top down SEMs that are representative of photoelectrodeposits generated using simultaneous illumination with a LED source with λ_{avg} = 775 nm polarized vertically and a LED source with λ_{avg} = 630 nm polarized horizontally, with intensity ratios between the two sources ($I_{\lambda=775;vert}/I_{\lambda=630;horiz}$) of 1.0 (a), 2.0 (b), 6.5 (c), and 9.0 (d), respectively. In (a), a lamellar structure was observed in which the long axes of the lamellae were oriented horizontally. The SEM in (b) is similar to that in (a) but displays a small amount of contrast in the spaces between the horizontally running lamellae. In (c), a lamellar structure in which the long axes of the lamellae are oriented vertically is observed. This structure exhibited a larger periodicity than those in (a) and (b). Also, vertically periodic contrast was observed in the space between the lamellae, suggesting the presence of a second set of intersecting lamellae having long axes oriented along the horizontal direction. In (d), like (c), a lamellar structure in which the long axes of the lamellae were oriented vertically was observed, and again the periodicity of this structure was greater than that observed in (a) or (b). Some contrast is visible in the spaces between the vertically running lamellae, but unlike in (c) this contrast did not appear to be periodic. Figure 4e−h and i−l, respectively, present SEMs acquired from the same samples as in (a)−(d), but acquired in cross-sectional view by cleaving the substrate and film along the vertical (perpendicular to the polarization vector of the λ_{avg} = 630 nm illumination during growth), and along the horizontal (perpendicular to the polarization vector of the λ_{avg} = 775 nm illumination during growth), respectively. The cross sections in (e) and (f) depict horizontally oriented lamellae similar to those seen in (a) and

DOI: 10.1021/acsnano.5b05119
ACS Nano 2016, 10, 102−111

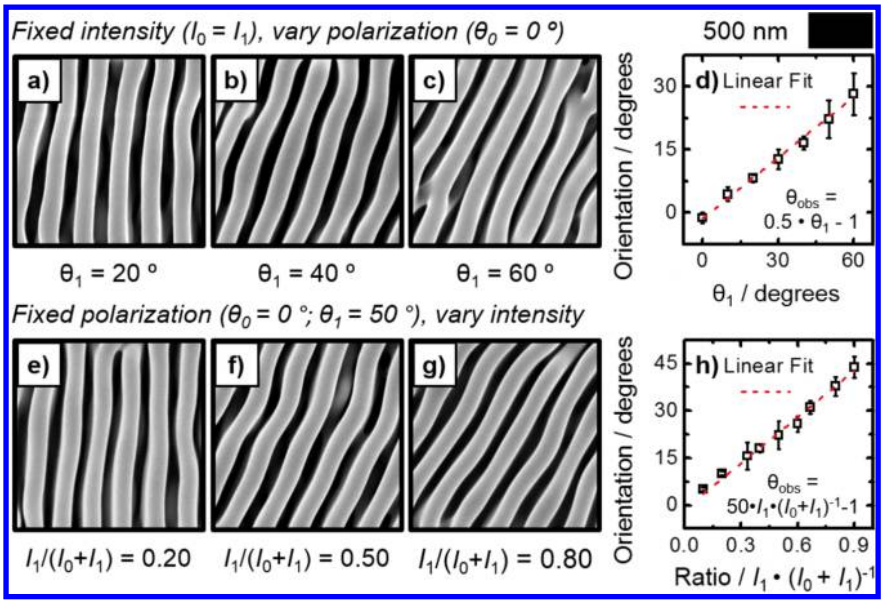

Figure 2. Pattern orientation in photoelectrodeposits generated using two same-wavelength (λ_{avg} = 630 nm) sources with differing linear polarizations. (a–c) SEMs representative of photoelectrodeposits generated using two sources with equal intensity, the first source polarized vertically ($\theta_0 = 0°$) and the second at the indicated rotation (θ_1) clockwise from the vertical. (d) Plot of the rotation of the orientation of the long axis of the pattern (θ_{obs}) measured clockwise from the vertical as a function of θ_1. (e–g) SEMs representative of photoelectrodeposits generated using two same-wavelength sources (λ_{avg} = 630 nm), each with a fixed linear polarization (first polarized vertically, the second offset $\theta_1 = 50°$ clockwise from the vertical) with the indicated fraction of the total intensity supplied by the second source $[I_1/(I_0 + I_1)]$. (h) Plot of θ_{obs} as a function of the fraction of the total intensity supplied by the second source.

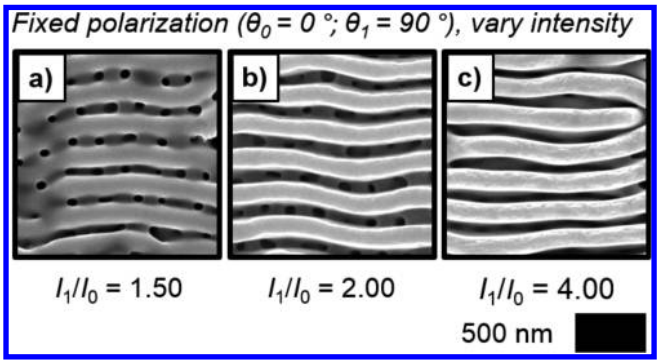

Figure 3. (a–c) SEMs representative of the photoelectrodeposits generated using two same-wavelength (λ_{avg} = 630 nm), orthogonally polarized sources (first polarized vertically, second horizontally) with the indicated intensity ratio between the horizontally and vertically polarized sources (I_1/I_0).

(b) from a perspective looking down the lamellar axes. In (g), a shorter, less well-defined structure similar to those observed in (e) and (f) and with a similar periodicity was observed superimposed on a mostly featureless ridge that is the side of a vertically running lamella similar to those observed in the top down micrograph in (c). In (h), the micrograph reveals a ridge that is also the side of a vertically running lamella, as in (g). Some superimposed growth is again observed, with a varying height from left to right across the micrograph. In (i), the micrograph reveals a ridge that is the side of a horizontally running lamella similar to those presented in the top down micrograph in (a). In (j), a ridge similar to that observed in (i) is displayed. Superimposed on this ridge is growth with periodically varying height from left to right across the micrograph. The cross sections in (k) and (l) depict vertically oriented lamellae similar to those seen in (c) and (d), from a perspective looking down the lamellar axis.

Point dipole radiation sources were used to model the amplitude modulation of the electric field at the active film–solution interface during photoelectrochemical growth that was caused by the inherent surface roughness of the deposited film. The time-averaged field amplitude resulting from two coherent dipole sources was calculated using two-dimensional finite-difference time-domain (FDTD) simulations. Figure 5 presents the normalized time-average of the electric-field magnitude from two dipoles emitting radiation with a free-space wavelength of λ = 630 nm in a medium of index n = 1.33 wherein the dipoles are separated by a distance of two wavelengths. In (a), the dipoles are separated perpendicular to the oscillation axis and from left to right three strong vertically running interference fringes are observed in the area between the dipoles. In (b), the dipoles are separated parallel to the oscillation axis, and constructive interference between the dipoles was not observed. Figure 6 presents simulations similar to those in Figure 5 but with two incoherently summed sets of coherent dipole pairs each aligned perpendicular to a direction of oscillation. In (a), one dipole set is separated along the horizontal axis while the axis of separation of the other set is rotated $\theta = 20°$ clockwise from the horizontal, and both sets emit radiation with equal intensity. Interference fringes similar to those displayed in Figure 5a were observed but were rotated clockwise from the vertical by $\theta_{obs} = 10°$. In (b), one dipole set is separated along the horizontal axis while the axis of separation of the other set is rotated $\theta = 50°$ clockwise from the horizontal, and the two sets emit radiation with a relative intensity $I_{rotated}/(I_{rotated} + I_{horizontal}) = 0.2$. Interference fringes similar to those in (a) were observed, and the most intense parts of the fringes were measured to be rotated clockwise from the vertical by $\theta_{obs} = 9°$.

Computer modeling of the photoelectrochemical growth process was performed to analyze the morphologies expected for films generated as a result of the fundamental light-matter

DOI: 10.1021/acsnano.5b05119
ACS Nano 2016, 10, 102–111

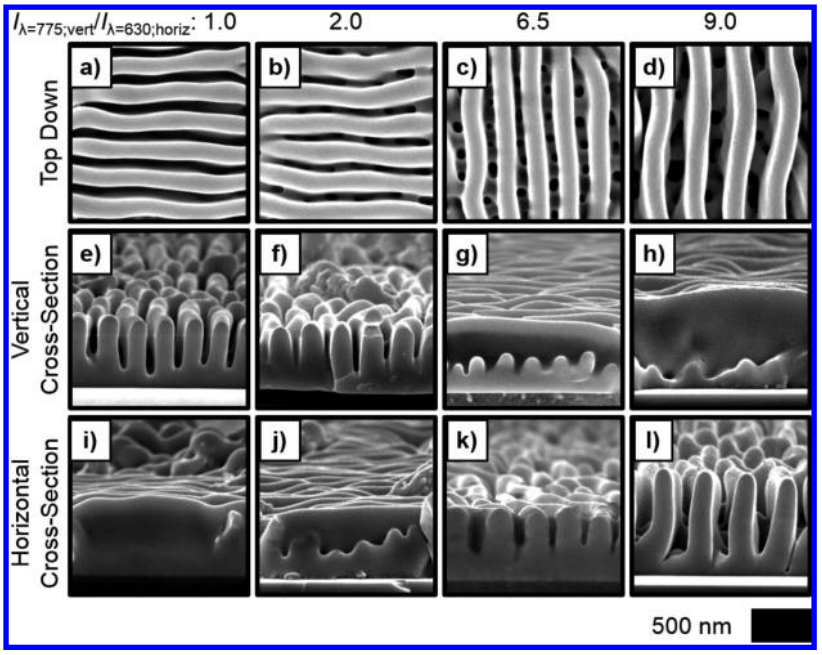

Figure 4. (a–d) Representative SEMs acquired in top down view of photoelectrodeposits generated using simultaneous illumination from a horizontally polarized λ_{avg} = 630 nm source and a vertically polarized λ_{avg} = 775 nm source with the indicated intensity ratio between the sources ($I_{\lambda=630;horiz}/I_{\lambda=780;vert}$). (e–h) Same as (a–d) but cleaved along the vertical axis (perpendicular to the polarization of the λ_{avg} = 630 nm illumination) and acquired in cross section. (i–l) Same as (a)–(d) but cleaved along the horizontal axis (perpendicular to the polarization of the λ_{avg} = 775 nm illumination) and acquired in cross section.

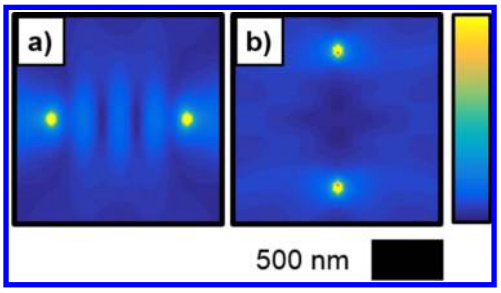

Figure 5. Normalized time-average of electric field magnitude from two dipoles emitting radiation with a free space wavelength of λ = 630 nm in a medium of index n = 1.33. Dipoles separated by a distance of two wavelengths in the direction (a) perpendicular and (b) parallel to the oscillation axis.

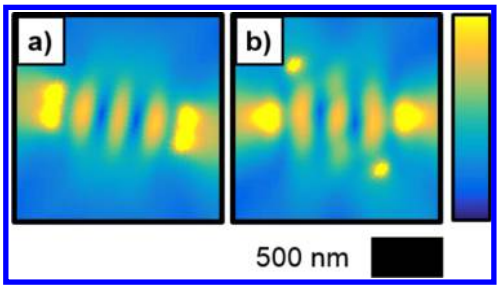

Figure 6. Normalized time-average of electric field magnitude resulting from two incoherently summed sets of dipole pairs each aligned perpendicular to a direction of oscillation. Dipoles are emitting radiation with a free space wavelength of λ = 630 nm in a medium of index n = 1.33. (a) One dipole set separated by two wavelengths along the horizontal axis and the axis of separation of the other set is rotated θ = 20° clockwise from the horizontal, both sets emit radiation with equal intensity. (b) One dipole set separated by two wavelengths along the horizontal axis and the axis of separation of the other set is rotated by θ = 50° clockwise from the horizontal, and the two sets emit radiation with relative intensity $I_{rotated}/(I_{rotated} + I_{horizontal})$ = 0.2.

interactions during the deposition, using simultaneous illumination with two same-wavelength sources having different linear polarizations. A two-step, iterative model was utilized wherein electromagnetic simulations were first used to calculate local photocarrier generation rates at the electrode/solution interface. In the second step, electrochemical mass addition was simulated via a Monte Carlo method that utilized the local photocarrier generation rate to weight the local probabilities of mass addition (see Methods section for further details). The only empirical data used in the simulations were literature-derived estimates of the complex index of refraction, the charge-carrier concentrations, and the excited state lifetimes, of the electrodeposited Se–Te material, and the refractive index of the solution. During the early stages of deposition, dipole sources could be used to represent pointlike scattering features due to surface roughness of the deposit and help to visualize the periodic absorption profile that occurs between two scattering features along the growth front. However, at later times, these interfacial features evolved into anisotropic structures that had an extended spatial structure. Utilization of the modeling algorithm, which recalculated the scattering and absorption profile as the film morphology evolved, enabled the growth process to be fully reproduced. Although computationally expensive, the two step growth model both incorporated the absorption modulation resulting from surface roughness during the early stages of growth and also captured the dynamic feedback between light absorption and material growth which resulted in 3D structures that agreed with experiment.

The experiment described in Figure 2a–d was simulated, wherein two equal intensity sources with λ_{avg} = 630 nm were utilized and one source was polarized vertically while the polarization of the second source was offset clockwise from the

DOI: 10.1021/acsnano.5b05119
ACS Nano 2016, 10, 102–111

vertical by θ_1, and the observed rotation of the long-axis of the lamellar pattern clockwise away from the vertical (θ_{obs}) was derived. Figure 7a presents a plot of both the experimentally

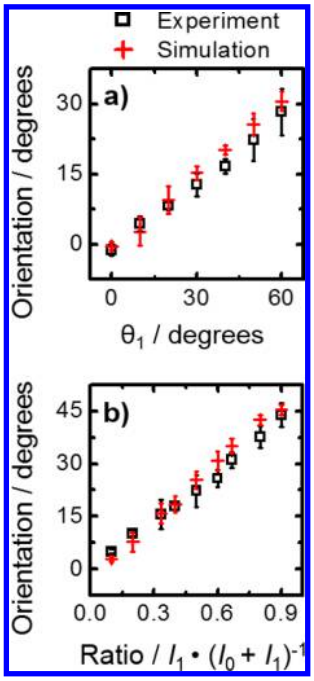

Figure 7. (a) Plot of the observed rotation of the orientation of the long-axis of the pattern (θ_{obs}) measured clockwise from the vertical as a function of the rotation of the polarization of one source (θ_1) in two-source illuminated photoelectrodepositions with same-wavelength (λ_{avg} = 630 nm), equal intensity sources when the other source was polarized vertically (θ_0 = 0°). (b) Plot of θ_{obs} as a function of the fraction of the total intensity [$I_1/(I_0 + I_1)$] delivered by a source polarized linearly θ_1 = 50° clockwise from the vertical in two-source illuminated photoelectrodepositions with same-wavelength sources when the other source was polarized vertically. Data points corresponding to experimental results as well as results derived computationally from growth modeling are presented.

and computationally derived values of θ_{obs} as a function of θ_1. The experiment described in Figure 2e–h was also simulated, wherein the two sources with λ_{avg} = 630 nm were again utilized, with one source polarized vertically and the other at θ_1 = 50° from the vertical in the clockwise direction, while the fraction of the total intensity delivered by the second source [$I_1/(I_0 + I_1)$] was varied. Figure 7b presents a plot of both the experimentally and computationally derived values of θ_{obs} for this experiment as a function of [$I_1/(I_0 + I_1)$]. For both experiments, the empirically and computationally derived values of θ_{obs} were in good agreement, and were linear functions of either θ_1 or [$I_1/(I_0 + I_1)$].

Additionally, computer modeling of the growth process was also performed to simulate the morphologies expected for films generated using simultaneous illumination from two orthogonally polarized, same-wavelength sources with unequal intensities. The experiment described in Figure 3(a)-(c) was modeled (Figure 8), wherein two unequal intensity sources with λ_{avg} = 630 nm were utilized with one source polarized vertically and the other horizontally. The intensity ratio between the horizontally polarized source and the vertically polarized source (I_1/I_0) was 1.50 (a), 2.00 (b), and 4.00 (c). The simulated morphologies were in close accord with those

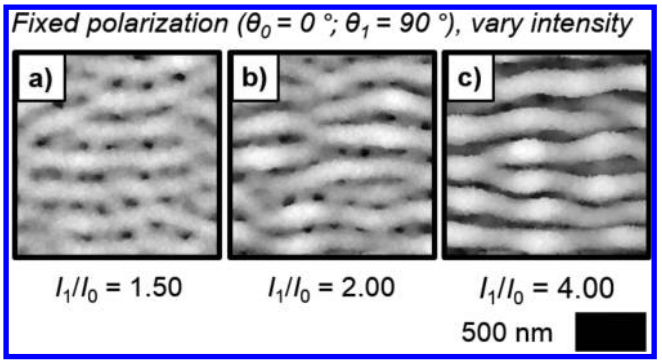

Figure 8. (a–c) Simulated morphologies of photoelectrodeposits generated using two same-wavelength (λ_{avg} = 630 nm), orthogonally polarized sources (first polarized vertically, second horizontally) with the indicated intensity ratio between the horizontally and vertically polarized sources (I_1/I_0).

observed experimentally (Figure 3), producing a square mesh morphology wherein the horizontally oriented lamellae were taller than those oriented vertically for I_1/I_0 = 1.50 and 2.00, and producing a single, horizontally oriented lamellar morphology for I_1/I_0 = 4.00.

To further understand the growth of the morphologies that were observed when two orthogonally polarized sources of differing intensities and/or wavelengths were utilized, three sets of simulations of light absorption in idealized intersecting lamellar features were performed. First, films that had been experimentally photoelectrodeposited under vertically polarized λ_{avg} = 630 nm illumination alone and 775 nm illumination alone were analyzed using SEM to derive the lamellar periods and widths of the resultant structures. These values were then used as the inputs for the lengths and widths of the idealized structures. Two idealized lamellae were oriented so as to intersect at a 90° angle and were assigned heights of 200 and 400 nm. In the first set of simulations, designed to help understand the growth of the morphologies that were observed when two orthogonally polarized sources with the same wavelength were used (λ_{avg} = 630 nm; Figure 3), the two lamellae both had widths that corresponded to the width of the lamellar structures observed for deposition with λ_{avg} = 630 nm illumination alone, and both had lengths equal to the corresponding lamellar period. Figure 9 presents the power absorption profile calculated (a) from a single λ = 630 nm plane wave source polarized parallel to the long axis of the taller lamella and (b) from two λ = 630 nm plane wave sources wherein one source was polarized parallel and the other perpendicular to the long axis of the taller lamella, with the source polarized perpendicular having half the intensity of the one polarized parallel. Figure 9a shows that significant absorption was observed only near the tip of the taller lamella. Figure 9b indicates that absorption was observed both at the tip of the taller lamella as well as at the tip of the shorter lamella.

The second and third sets of light absorption simulations were designed to help understand the generation of the morphologies observed when two orthogonally polarized sources with λ_{avg} = 630 nm and λ_{avg} = 775 nm were utilized simultaneously (Figure 4). In the second set of simulations, the taller lamellar feature had a width corresponding to the width of the lamellar structures observed for deposition with λ_{avg} = 630 nm illumination alone, and the length of the shorter lamella was equal to the corresponding lamellar period. The shorter lamellar feature had a width corresponding to the width of

DOI: 10.1021/acsnano.5b05119
ACS Nano 2016, 10, 102–111

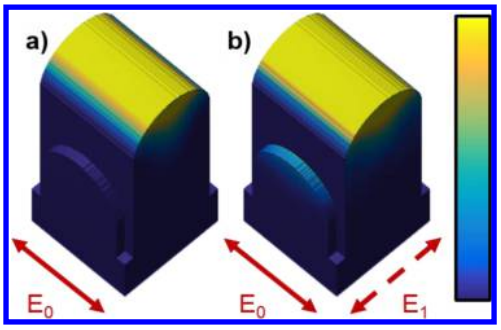

Figure 9. (a) Simulated power absorption of two idealized, orthogonal lamellae under a λ = 630 nm plane wave source polarized parallel to the taller feature (E_0). The width of each structure is typical of lamellar structures generated via photoelectrodeposition with λ_{avg} = 630 nm illumination, and the length of each lamella is typical of one period of such structures. (b) Same as (a) but with the addition of a second λ = 630 nm source with half the intensity of the first and polarized perpendicular to the taller feature (E_1) (sources assumed to be incoherent).

the lamellar structures observed for deposition with λ_{avg} = 775 nm illumination alone, and the length of the taller lamella was equal to the corresponding lamellar period. Figure 10a and b, respectively, present the power absorption profile calculated from a single λ = 630 nm plane-wave source polarized parallel to the long axis of the taller lamella alone, and from the same source as in (a) as well as a secondary λ = 775 nm plane-wave source polarized perpendicular to the long axis of the taller lamella that was twice as intense as the λ = 630 nm source. In Figure 10a, significant absorption was observed only near the tip of the taller lamella. In Figure 10b, absorption was observed both at the tip of the taller lamella as well as at the tip of the shorter lamella. The third set of simulations utilized lamellar structures having similar dimensions as the second set but with the heights of the two lamellae exchanged. Figure 10c and d, respectively, present the power absorption profile calculated from a single λ = 775 nm plane-wave source polarized parallel to the long axis of the taller lamella alone and from the same source as in (c) as well as a secondary λ = 630 nm plane wave source polarized perpendicular to the long axis of the taller lamella that was 6.5 times less intense than the λ = 775 nm source. As with the second set of simulations (Figure 10a, b) in Figure 10c, significant absorption was observed only near the tip of the taller lamella, whereas in Figure 10d absorption was observed both at the tip of the taller lamella as well as at the tip of the shorter lamella.

DISCUSSION

When two sources having the same wavelength (λ_{avg} = 630 nm) but having differing, linear, nonorthogonal polarizations were utilized simultaneously (Figure 2a–c and e–g), a lamellar pattern identical to those observed with only a single source (Figure 1) was observed, except for an in-plane rotation. This result can be readily understood because any linear polarization can be equivalently expressed as the sum of two orthogonal linear polarizations, for example, vertical and horizontal. Thus, no difference may be observed between the morphology generated if a single illumination source is utilized relative to the morphology generated if two sources are used simultaneously, as long as the intensity-weighted average of the polarization orientations of the two tandem sources is the same as the polarization of the single source. The experimental data

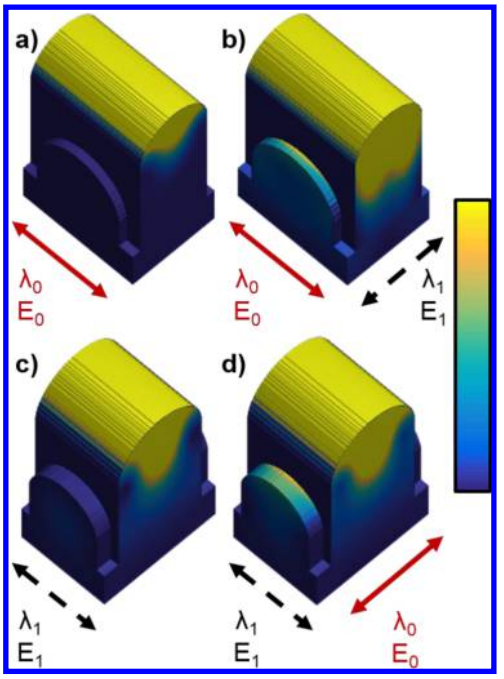

Figure 10. (a) Simulated power absorption of two idealized, orthogonal lamellae under a λ_0 = 630 nm plane wave source polarized parallel to the taller feature (E_0). The width of the taller structure is typical of lamellar structures generated via photoelectrodeposition with λ_{avg} = 630 nm illumination whereas the width of the shorter structure is typical of the structures generated with λ_{avg} = 775 nm illumination. (b) Same as (a) but with the addition of a λ_1 = 775 nm plane wave source 2 times more intense than the 630 nm source and polarized perpendicular to the taller feature (E_1) (sources assumed to be incoherent). (c) Simulated power absorption of two idealized, orthogonal lamellae under a λ_1 = 775 nm plane wave source polarized parallel to the taller feature (E_1). The width of the taller structure is typical of lamellar structures generated via photoelectrodeposition with λ_{avg} = 775 nm illumination whereas the width of the shorter structure is typical of the structures generated with λ_{avg} = 630 nm illumination. (d) Same as (c) but with the addition of a λ_0 = 630 nm plane wave source 6.5 times less intense than the 775 nm source and polarized perpendicular to the taller feature (E_0) (sources assumed to be incoherent).

quantitatively supports this hypothesis, because the observed orientation of the pattern (θ_{obs}) for the two-source experiments was almost exactly equal to the intensity-weighted average polarization orientation: $(I_0\theta_0 + I_1\theta_1)/(I_0 + I_1)$. For the experiment wherein the intensity of the sources was equal ($I_0 = I_1$), the first source was polarized vertically ($\theta_0 = 0°$) and the angle between the polarization vectors (θ_1) was varied, θ_{obs} would be expected to have the form $0.5\theta_1$. This expectation is very close to the experimentally observed relation of $\theta_{obs} = 0.5\theta_1 - 1$. Similarly, for the experiment in which the polarizations of the two sources were fixed ($\theta_0 = 0°$ and $\theta_1 = 50°$) and the relative contribution of the two sources to the total intensity was varied, θ_{obs} would be expected to have the form $50[I_1/(I_0 + I_1)]$, which again is very close to the experimentally observed relation of $\theta_{obs} = 50[I_1/(I_0 + I_1)] - 1$. The difference between the expected and experimentally observed relations for θ_{obs}, a $-1°$ offset, is likely a minor systematic error arising from a minor calibration error in a polarizer setting. This notion is supported by the facts that a value of $\theta_{obs} = -1 \pm 1°$ was observed when $\theta_0 = \theta_1 = 0°$, and

DOI: 10.1021/acsnano.5b05119
ACS Nano 2016, 10, 102–111

that the experimentally observed values of θ_{obs} were generally marginally lower than expected.

The quantitative agreement between the values of θ_{obs} measured in the experiments using same-wavelength (λ_{avg} = 630 nm) sources with mutually different linear, nonorthogonal polarizations simultaneously, and in the analogous computer simulations (Figure 7), which utilized minimal empirical data, for all investigated conditions, suggests that the empirically observed behavior is the result of a fundamental optical phenomenon. This notion is supported by the results of the dipole scattering simulations (Figures 5 and 6). The interference fringes observed between two simulated radiation-emitting dipoles separated along the horizontal axis, and perpendicular to the oscillation axis (Figure 5a), are reminiscent of the lamellar morphology observed in the photoelectrodeposit generated with vertically polarized illumination (Figure 1a), and have been hypothesized to promote the initial growth of this periodic and anisotropic structure by providing the necessary spatially varying distribution of light intensity.[14] When two sets of dipoles were simulated with some angle, θ, between their axes of separation, the resultant interference fringes were observed to rotate by an angle, θ_{obs}, that is in good agreement with relation of $\theta_{obs} = \theta[I_{rotated}/(I_{rotated} + I_{horizontal})]$. Thus, the dipole scattering simulations suggest that the orientation of the lamellar structures in the nonorthogonal, same-wavelength experiments is a manifestation of the elementary phenomenon of superposition of waves.

When two orthogonally polarized same-wavelength (λ_{avg} = 630 nm) sources that had unequal mutual intensities were utilized, the resultant structures appeared to consist of two intersecting sets of orthogonally oriented lamellae wherein the relative heights of each set of lamellae were directly proportional to the relative source intensities (Figure 3). These observations indicate that the utilization of orthogonally polarized sources can enable independent control over different features of the resultant film morphology, and thus comprises a potentially useful tool for generating application-specific structures. The reproduction of the experimental morphologies by the growth model (Figure 8) suggests that the generation of the intersecting structures when orthogonally polarized light is used is a result of the intrinsic light−matter interactions that occur during the deposition process. Moreover, the continued growth of such intersecting structures under the aforementioned conditions is consistent with the simulations of light absorption in the idealized versions of the structures (Figure 9) wherein illumination from two orthogonally polarized sources is preferentially absorbed in the tips of both structures. These areas represent the photoelectrochemical growth fronts: preferential light absorption in these areas supports continued anisotropic growth in a manner that preserves the cross sections of the features. Furthermore, visualization of the difference in the absorption profile with and without the contribution from the source parallel to the shorter feature indicated that this source was solely responsible for absorption along the shorter feature.

Intersecting lamellar structures were also observed when two orthogonally polarized sources with differing wavelengths (λ_{avg} = 630 and 775 nm) were utilized. Again, the relative heights of each set of lamellae were proportional to the relative source intensities. However, for $I_{\lambda=775;vert}/I_{\lambda=630;horiz}$ = 1.0, SEM analysis provided little evidence for the presence of periodic, anisotropic structures with long axes oriented along the vertical, and, for $I_{\lambda=775;vert}/I_{\lambda=630;horiz}$ = 2.0, such structures were found to be shorter than the simultaneously observed, horizontally oriented structures. Also, for $I_{\lambda=775;vert}/I_{\lambda=630;horiz}$ = 6.5 and 9.0, structures with horizontal periodicity were observed. These observations are consistent with previous physical characterization suggesting lower rates of photoelectrodeposition may be observed when utilizing λ = 775 nm illumination than when utilizing λ = 630 nm illumination. The nanocrystalline nature of the photoelectrodeposited films suggests free carriers generated near the solution interface may contribute to the deposition of additional material in a disproportionally large manner as free carriers generated in the bulk have a greater probability of recombining before reaching the interface. The electromagnetic penetration depth of a material is inversely proportional to the imaginary component of its complex refractive index, κ. Spectroscopic ellipsometry measurements have shown that photoelectrodeposited Se−Te films exhibit monotonically decreasing values of κ with increasing values of λ for λ = 450 to 850 nm.[14] Thus, for lower values of λ, it is expected that more free carriers will be generated near the solution interface, correlating to a higher deposition rate.

Unlike the intersecting lamellar structures generated using two orthogonally polarized same-wavelength sources (λ_{avg} = 630 nm), when two orthogonally polarized sources with differing wavelengths (λ_{avg} = 630 and 775 nm) were used, the periodicities of the two sets of lamellae were unequal. The set with their long axes oriented parallel to the polarization vector of the λ_{avg} = 775 nm source displayed a greater periodicity than those oriented parallel to the polarization vector of the λ_{avg} = 630 nm source. This difference in periodicity is a consequence of differing anisotropic light absorption profiles in the growing structures in response to the different wavelengths which cause the lamellar period to increase monotonically with λ.[14] Moreover, these results indicate that not only is it possible to control the relative heights of structures with orthogonal periodicities, but also indicate that the magnitudes of those periodicities can also be controlled, which may be of use in the construction of purpose-designed structures. Simulations in idealized versions of these intersecting structures were again consistent with their growth (Figure 10): illumination polarized along the long axis of a lamellar structure (of the same wavelength used to generate that structure) is preferentially absorbed in the tip of that structure relative to light polarized perpendicularly (of a different wavelength).

Dynamic photoelectrochemical growth may find potential in the generation of nanophotonic optical elements including planar lenses and mirrors,[21−23] polarization-sensitive filters and photodetectors,[24] and nanostructured scaffolds.[25,26] The results described in this work have several implications for the use of this process to design application-targeted structures. First, controlling the pattern orientation with respect to the substrate does not require changing the polarization state of a single source, for example, rotating a linear polarizer. Instead, two sources could be used with static linear polarizations and the pattern orientation could be controlled by changing the relative intensity of the sources. Manipulating such a quantity continuously or in discrete steps over time could be used to generate morphological complexity. The utilization of orthogonal sources also presents another method to generate intricate structures wherein control of the feature size in three dimensions of two patterns may be obtained simultaneously and independently.

DOI: 10.1021/acsnano.5b05119
ACS Nano 2016, 10, 102−111

CONCLUSIONS

Nanopatterned Se−Te films were photoelectrochemically prepared using simultaneous illumination from two light sources with discrete linear polarizations. Films grown with two nonorthogonally polarized, same-wavelength sources displayed lamellar morphologies wherein the long axes of the structures were aligned along the intensity-weighted average polarization vector. Such behavior was consistent with simulations of light scattering at the solution-film interface at the onset of photoelectrochemical growth. Simulations of the growth with such illumination showed that the emergence of the observed morphologies could be understood by considering the fundamental light-matter interactions during deposition. Structures consisting of two sets of intersecting, orthogonal lamellae were generated when two orthogonally polarized illumination sources were utilized wherein the periodicity and feature size of each set of lamellae was proportional to the wavelengths of the illumination source polarized along their long axes. The evolution of such morphologies was consistent with simulations of light absorption in idealized intersecting lamellar structures, which indicated that the lamellae preferentially absorbed light polarized with the electric field vector parallel to their long axes. The cumulative data suggests that under the conditions investigated, the morphology of the photoelectrodeposit is sensitive simultaneously to the polarization of both sources utilized during growth. Additionally, the use of such tailored optical excitation provides control over the pattern orientation and enables the generation of three-dimensional structures that cannot be produced with a single polarization.

METHODS

Materials and Chemicals. $(CH_3)_2CO$ (ACS grade, BDH), CH_3OH (ACS grade, EMD), H_2SO_4 (ACS Reagent, J. T. Baker), HF (49%, Semiconductor grade, Puritan Products), In (99.999%, Alfa Aesar), Ga (99.999%, Alfa Aesar), SeO_2 (99.4%, Alfa Aesar), and TeO_2 (99+ % Sigma-Aldrich) were used as received. H_2O with a resistivity of ≥18.2 MΩ cm (Barnstead Nanopure System) was used throughout. n^+-Si(111) (0.004−0.006 Ω cm, As-doped, 400 ± 15 μm, single-side polished, Addison Engineering) was used as a substrate for deposition. Flash-Dry Silver Paint (SPI Supplies), Double/Bubble Epoxy (Hardman), and nitrocellulose-based nail polish were used to assemble the Si working electrodes.

Electrode Preparation. One end of a Sn-coated Cu wire (22 AWG) was bent to form a small, flat coil and the wire was then threaded through glass tubing (6 mm O. D.) such that the coil was just outside the tubing. Epoxy was applied to seal the end of the tube from which the coil protruded. Square Si wafer sections (ca. 5 mm by 5 mm) were cut, and a eutectic mixture of Ga and In was scratched into the unpolished surfaces with a carbide scribe. The wire coil was then contacted to the unpolished surface and affixed with Ag paint. Nail polish was applied to insulate the unpolished face, the wire−coil contact, and the exposed wire between the coil and epoxy seal. Immediately before deposition, the Si surface of each electrode was clean sequentially with $(CH_3)_2CO$, CH_3OH and H_2O, and then the Si section of the electrode was immersed in a 49 wt % solution of HF(aq) for ∼10 s to remove any SiO_x present at the surface of the Si. The electrode was then rinsed with H_2O and dried under a stream of N_2(g).

Photoelectrochemical Deposition. Photoelectrochemical deposition was performed using a Bio-Logic SP-200 potentiostat. Deposition was performed in a single-compartment glass cell with a pyrex window. A three-electrode configuration was utilized with a graphite-rod counter electrode (99.999%, Sigma-Aldrich) and a Ag/AgCl reference electrode (3 M KCl, Bioanalytical Systems). Films were deposited from an aqueous solution of 0.0200 M SeO_2, 0.0100 M TeO_2, and 2.00 M H_2SO_4. Deposition was effected by biasing the illuminated n^+-Si electrode potentiostatically at −0.40 V vs Ag/AgCl for 5.00 min at room temperature. After deposition, the electrode was immediately removed from the cell, rinsed with H_2O, and then dried under a stream of N_2(g). The Si substrate with a top-facing Se−Te film was mechanically separated from the rest of the electrode assembly. The nitrocellulose-based insulation, as well as the majority of the Ag paint and In−Ga eutectic, were then removed mechanically.

Electrode Illumination. The illumination utilized during photoelectrochemical deposition was provided by narrowband diode (LED) sources (Thorlabs) with respective intensity-weighted λ_{avg} values and spectral bandwidths (fwhm) of 630 and 18 nm (M625L2 or M625L3), and 775 and 31 nm (M780L2). The output of each diode source was collected and collimated with an aspheric condenser lens (Ø30 mm, f = 26.5 mm). For experiments involving simultaneous illumination with the two 630 nm sources, a polka dot beam splitter (Thor Laboratories BPD508-G) was utilized to combine the outputs. Both sources were incident upon the beamsplitter at an angle of 45° from the surface normal and thus generated coaxial output. For experiments involving simultaneous illumination with a 630 nm source and a 775 nm source, a dichroic filter (Edmund Optics #69-219) was utilized in the same geometry that was utilized for combining two same-wavelength sources with the beam splitter. A dichroic film polarizer (Thorlabs LPVISE2X2 or LPNIRE200-B) was placed between each source and the appropriate combining optic to enable independent control of the polarization of each source. The 775 nm source was used exclusively with the LPNIRE200-B polarizer. A 1500 grit ground-glass (N-BK7) diffuser was placed immediately in front of the photoelectrochemical cell to ensure spatial homogeneity of the illumination. The light intensity incident on the electrode was measured by placing a calibrated Si photodiode (Thorlabs FDS100) in place of an electrode assembly in the photoelectrochemical cell with electrolyte, and measuring the steady-state current response of that Si photodiode. Depositions utilizing a single diode with λ_{avg} = 630 nm or two such diodes simultaneously to provide illumination were performed with a total light intensity of 13.7 mW cm^{-2} at the electrode. Depositions utilizing the diodes with λ_{avg} = 630 and 775 nm in conjunction were performed with a total light intensity of 30.0 mW cm^{-2}.

Microscopy. SEMs were obtained with a FEI Nova NanoSEM 450 at an accelerating voltage of 5.00 kV with a working distance of 5 mm and an in-lens secondary electron detector. Micrographs obtained for quantitative analysis were acquired with a resolution of 172 pixels μm^{-1} over ca. 120 μm^2 areas. Micrographs utilized to produce display figures were acquired with a resolution of 344 pixels μm^{-1} over *ca.* 8 μm^2 areas.

Simulation of Film Morphology. The growths of the photoelectrochemically deposited films were simulated with an iterative growth model wherein electromagnetic simulations were first used to calculate the local photocarrier-generation rates at the film surface. Then, mass addition was simulated via a Monte Carlo method wherein the local photocarrier-generation rate weighted the local rate of mass addition along the film surface.

Growth simulations began with a bare, semi-infinite planar Si substrate. In the first step, the light-absorption profile under one or two linearly polarized, plane-wave illumination source(s) was calculated using full-wave finite-difference time-domain (FDTD) simulations with periodic boundary conditions along the substrate interface. In the second step, a Monte Carlo simulation was performed in which an amount of mass, equaling that of a 10 nm planar layer that covered the simulation area, was added to the upper surface of the structure with a probability F:

$$F(G) = \left[1 + G(n_0\tau_p + p_0\tau_n) + G^2\frac{\tau_p\tau_n}{n_i^2}\right]\prod_{i=1}^{3}\frac{x_i}{r_i} \quad (1)$$

where G is the spatially dependent photocarrier generation rate at the deposit-solution interface, n_i is the intrinsic carrier concentration, n_0 is the electron concentration, p_0 is the hole concentration, τ_n is the electron lifetime, τ_p is the hole lifetime, x_i is the fraction of ith nearest neighbors occupied in the cubic lattice, and r_i is the distance to the ith

DOI: 10.1021/acsnano.5b05119
ACS Nano 2016, 10, 102−111

nearest neighbor. The product in the definition of this probability (eq 1) serves to reduce the surface roughness of the film so as to mimic the experimentally observed surface roughness.

After the initial Monte Carlo simulation, the absorbance of the new, structured film was then calculated in the same manner as for the initial planar film, and an additional Monte Carlo simulation of mass addition was performed. This process of absorbance calculation and mass addition was repeated for a total of 30 iterations.

General Parameters for Computational Modeling. Se−Te films were assumed to be undoped (*i.e.*, $n_0 = p_0 = n_i$) and a value of $n_i = 10^{10}$ cm^{-3} was used for the intrinsic carrier concentration.[27] A value of 1 μs was used for both the electron and hole carrier lifetimes.[28] A value of $n = 1.33$ was used for the refractive index of the electrolyte regardless of wavelength.[29] Previously measured values of the complex index of refraction for Se−Te were utilized.[14] Illumination intensities identical to those used experimentally (see above) were used in the simulations. The electric field vector of the illumination was oriented parallel to the substrate. All FDTD simulations were performed using the "FDTD Solutions" software package (Lumerical).

Simulations of Dipole Emitters. The time-averaged field amplitude resulting from two coherent dipole sources was calculated using two-dimensional FDTD simulations. For simulations representing two illumination sources with different polarizations, the field amplitude profile was rotated about the simulation center and summed with the original field amplitude. A two-dimensional square simulation mesh with a lattice constant of 14 nm was used.

Simulated Absorption Profile of Idealized Intersecting Lamella. Three-dimensional FDTD simulations were used to calculate the normalized absorption profile of two intersecting idealized lamellar features. A three-dimensional cubic simulation mesh with a lattice constant of 2 nm was used. The idealized structure, from bottom to top, consisted of a semi-infinite Si substrate, a 100 nm conformal Se−Te layer, and two Se−Te lamellae with hemispherical upper boundaries. The lamellae were either 200 or 400 nm tall as indicated in the main text, as measured from the upper boundary of the conformal layer.

AUTHOR INFORMATION

Corresponding Author

*E-mail: nslewis@caltech.edu.

Notes

The authors declare no competing financial interest.

ACKNOWLEDGMENTS

This work was supported by the "Light-Material Interactions in Energy Conversion" Energy Frontier Research Center funded by the U.S. Department of Energy, Office of Science, Office of Basic Energy Sciences under Award Number DE-SC0001293. The authors gratefully acknowledge R. Gerhart for assistance with photoelectrochemical cell fabrication. A.I.C. recognizes a Graduate Research Fellowship from the National Science Foundation for support. A.P. recognizes an Edward W. Hughes Research Fellowship from the California Institute of Technology for support.

REFERENCES

(1) Chen, G.; Imanishi, Y.; Ito, Y. pH-Sensitive Thin Hydrogel Microfabricated by Photolithography. *Langmuir* **1998**, *14*, 6610−6612.

(2) Revzin, A.; Russell, R. J.; Yadavalli, V. K.; Koh, W.-G.; Deister, C.; Hile, D. D.; Mellott, M. B.; Pishko, M. V. Fabrication of Poly(ethylene glycol) Hydrogel Microstructures Using Photolithography. *Langmuir* **2001**, *17*, 5440−5447.

(3) Totzeck, M.; Ulrich, W.; Göhnermeier, A.; Kaiser, W. Pushing Deep Ultraviolet Lithography to its Limits. *Nat. Photonics* **2007**, *1*, 629−631.

(4) Gibbons, W. M.; Shannon, P. J.; Sun, S.-T.; Swetlin, B. J. Surface-Mediated Alignment of Nematic Crystals with Polarized Laser Light. *Nature* **1991**, *351*, 49−50.

(5) Shannon, P. J.; Gibbons, W. M.; Sun, S.-T. Patterned Optical Properties in Photopolymerized Surface-Aligned Liquid-Crystal Films. *Nature* **1994**, *368*, 532−533.

(6) Ichimura, K. Photoalignment of Liquid-Crystal Systems. *Chem. Rev.* **2000**, *100*, 1847−1873.

(7) Barrett, C. J.; Natansohn, A. L.; Rochon, P. L. Mechanism of Optically Inscribed High-Efficiency Diffraction Gratings in Azo Polymer Films. *J. Phys. Chem.* **1996**, *100*, 8836−8842.

(8) Hubert, C.; Rumyantseva, A.; Lerondel, G.; Grand, J.; Kostcheev, S.; Billot, L.; Vial, A.; Bachelot, R.; Royer, P.; Chang, S.-h.; et al. Near-Field Photochemical Imaging of Noble Metal Nanostructures. *Nano Lett.* **2005**, *5*, 615−619.

(9) Hubert, C.; Bachelot, R.; Plain, J.; Kostcheev, S.; Lerondel, G.; Juan, M.; Royer, P.; Zou, S.; Schatz, G. C.; Wiederrecht, G. P.; et al. Near-Field Polarization Effects in Molecular-Motion-Induced Photochemical Imaging. *J. Phys. Chem. C* **2008**, *112*, 4111−4116.

(10) Plain, J.; Wiederrecht, G. P.; Gray, S. K.; Royer, P.; Bachelot, R. Multiscale Optical Imaging of Complex Fields Based on the Use of Azobenzene Nanomotors. *J. Phys. Chem. Lett.* **2013**, *4*, 2124−2132.

(11) Ishitobi, H.; Nakamura, I.; Kobayashi, T.-a.; Hayazawa, N.; Sekkat, Z.; Kawata, S.; Inouye, Y. Nanomovement of Azo Polymers Induced by Longitudinal Fields. *ACS Photonics* **2014**, *1*, 190−197.

(12) Paul, A.; Kenens, B.; Hofkens, J.; Uji-i, H. Excitation Polarization Sensitivity of Plasmon-Mediated Silver Nanotriangle Growth on a Surface. *Langmuir* **2012**, *28*, 8920−8925.

(13) Langille, M. R.; Personick, M. L.; Mirkin, C. A. Plasmon-Mediated Syntheses of Metallic Nanostructures. *Angew. Chem., Int. Ed.* **2013**, *52*, 13910−13940.

(14) Sadtler, B.; Burgos, S. P.; Batara, N. A.; Beardslee, J. A.; Atwater, H. A.; Lewis, N. S. Phototropic Growth Control of Nanoscale Pattern Formation in Photoelectrodeposited Se-Te Films. *Proc. Natl. Acad. Sci. U. S. A.* **2013**, *110*, 19707−19712.

(15) Yin, A. J.; Li, J.; Jian, W.; Bennett, A. J.; Xu, J. M. Fabrication of Highly Ordered Metallic Nanowire Arrays by Electrodeposition. *Appl. Phys. Lett.* **2001**, *79*, 1039.

(16) Sander, M. S.; Prieto, A. L.; Gronsky, R.; Stacy, A. M. Fabrication of High-Density, High Aspect Ratio, Large-Area Bismuth Telluride Nanowire Arrays by Electrodeposition into Porous Anodic Alumina Templates. *Adv. Mater.* **2002**, *14*, 665−667.

(17) Choi, K.-S.; Lichtenegger, H. C.; Stucky, G. D.; McFarland, E. W. Electrochemical Synthesis of Nanostructured ZnO Films Utilizing Self-Assembly of Surfactant Molecules at Solid-Liquid Interfaces. *J. Am. Chem. Soc.* **2002**, *124*, 12402−12403.

(18) Choi, K.-S. Shape Control of Inorganic Materials *via* Electrodeposition. *Dalton Trans.* **2008**, 5432−5438.

(19) Attard, A. E.; Brown, D. E. Photoelectroplating Light Modulator. *Appl. Opt.* **1968**, *7*, 511−516.

(20) Inoue, T.; Fujishima, A.; Honda, K. Photoelectrochromic Characteristics of Photoelectrochemical Imaging System with a Semiconductor/Solution (Metallic Ion) Junction. *J. Electrochem. Soc.* **1980**, *127*, 1582−1588.

(21) Kildishev, A. V.; Boltasseva, A.; Shalaev, V. M. Planar Photonics with Metasurfaces. *Science* **2013**, *339*, 1232009.

(22) Verslegers, L.; Catrysse, P. B.; Yu, Z.; White, J. S.; Barnard, E. S.; Brongersma, M. L.; Fan, S. Planar Lenses Based on Nanoscale Slit Arrays in a Metallic Film. *Nano Lett.* **2009**, *9*, 235−238.

(23) Fattal, D.; Li, J.; Peng, Z.; Fiorentino, M.; Beausoleil, R. G. Flat Dielectric Grating Reflectors with Focusing Abilities. *Nat. Photonics* **2010**, *4*, 466−470.

(24) Gansel, J. K.; Thiel, M.; Rill, M. S.; Decker, M.; Bade, K.; Saile, V.; von Freymann, G.; Linden, S.; Wegener, M. Gold Helix Photonic Metamaterial As Broadband Circular Polarizer. *Science* **2009**, *325*, 1513−1515.

(25) Chen, Z.; Cummins, D.; Reinecke, B. N.; Clark, E.; Sunkara, M. K.; Jaramillo, T. F. Core-shell MoO_3-MoS_2 Nanowires for Hydrogen

DOI: 10.1021/acsnano.5b05119
ACS Nano 2016, 10, 102−111

Evolution: A Functional Design for Electrocatalytic Materials. *Nano Lett.* **2011**, *11*, 4168−4175.
(26) Kong, D.; Wang, H.; Lu, Z.; Cui, Y. $CoSe_2$ Nanoparticles Grown on Carbon Fiber Paper: An Efficient and Stable Electrocatalyst for Hydrogen Evolution Reaction. *J. Am. Chem. Soc.* **2014**, *136*, 4897−4900.
(27) El-Korashy, A.; El-Zahed, H.; Zayed, H. A.; Kenawy, M. A. Effect of Composition and Structure on Electrical Conduction in $Se_{(100-x)}Te_{(x)}$ Films. *Solid State Commun.* **1995**, *95*, 335−339.
(28) Mott, N. F.; Davis, E. A. *Electronic Processes in Non-Crystalline Materials*, 2nd ed.; Oxford University Press: New York, 1971.
(29) Hale, G. M.; Querry, M. R. Optical Constants of Water in the 200-nm to 200-μm Wavelength Region. *Appl. Opt.* **1973**, *12*, 555−563.

DOI: 10.1021/acsnano.5b05119
ACS Nano 2016, 10, 102−111